CrossMark

Spectropolarimetric Observations of Solar Noise Storms at Low Frequencies

V. Mugundhan[1] · **R. Ramesh**[1] · **C. Kathiravan**[1] ·
G.V.S. Gireesh[1] · **Aathira Hegde**[2]

Abstract A new high-resolution radio spectropolarimeter instrument operating in the frequency range of $15-85$ MHz has recently been commissioned at the Radio Astronomy Field Station of the Indian Institute of Astrophysics at Gauribidanur, 100 km north of Bangalore, India. We describe the design and construction of this instrument. We present observations of a solar radio noise storm associated with Active Region (AR) 12567 in the frequency range of $\approx 15-85$ MHz during 18 and 19 July 2016, observed using this instrument in the meridian-transit mode. This is the first report that we are aware of in which both the burst and continuum properties are derived simultaneously. Spectral indices and degree of polarization of both the continuum radiation and bursts are estimated. It is found that

i) Type I storm bursts have a spectral index of $\approx +3.5$,
ii) the spectral index of the background continuum is $\approx +2.9$,
iii) the transition frequency between Type I and Type III storms occurs at ≈ 55 MHz,
iv) Type III bursts have an average spectral index of ≈ -2.7,
v) the spectral index of the Type III continuum is ≈ -1.6, and
vi) the degree of circular polarization of all Type I (Type III) bursts is $\approx 90\%$ (30%).

The results obtained here indicate that the continuum emission is due to bursts occurring in rapid succession. We find that the derived parameters for Type I bursts are consistent with suprathermal electron acceleration theory and those of Type III favor fundamental plasma emission.

Keywords Corona, radio emission · Polarization, radio · Radio bursts, meter-wavelengths and longer (m, dkm, hm, km) · Radio bursts, Type I · Radio bursts, Type III · Instrumentation and Data Management

✉ V. Mugundhan
mugundhan@iiap.res.in

1   Indian Institute of Astrophysics, 2nd Block, Koramangala, Bangalore, India

2   Indian Institute of Space Technology, Valiamala, Thiruvananthapuram, India

🖄 Springer

1. Introduction

Type I solar radio emission is the most frequently occurring form of solar radio activity. It consists of a broad-band, long-lived (few hours to days) background continuum, and narrow-band (few kHz – 4 MHz), short-lived (few seconds) bursts (Type I bursts, hereafter) that are superposed on the background continuum constitute Type I emission (Wild and McCready, 1950; Wild, 1951). The radiation is strongly circularly polarized (Payne-Scott, 1949; Ryle, 1948; Zlobec, 1971; Ramesh *et al.*, 2013) and is found to be always associated with an active region (McCready, Pawsey, and Payne-Scott, 1947; Hey, Parsons, and Phillips, 1948; Allen, 1947; Swarup, Stone, and Maxwell, 1960; Dodson, 1957), but there have been reports of coronal mass ejection (CME) association as well (Kerdraon *et al.*, 1983; Ramesh and Shanmugha Sundaram, 2001; Kathiravan, Ramesh, and Nataraj, 2007; Ramesh, Kathiravan, and Rajalingam, 2012).

Type I storm radiation has typically been observed in the frequency range of $\approx 50\,\mathrm{MHz}$ – 200 MHz and only on very rare occasions above or below this (Elgarøy, 1977). Close to frequencies ≈ 50–60 MHz, Type I storms transition to Type III storms. These Type III storms are also accompanied by continuum and bursts (de La Noe and Gergely, 1977). It has been suggested that the same electron population may be responsible for the generation of both categories of radio emission (Boischot, de La Noe, and Moller-Pedersen, 1970; Stewart and Labrum, 1972).

Spectropolarimetric observations of solar noise storms at low frequencies with high spectral and temporal resolutions have been relatively rare. Earlier observations (see Table 2.1 in Elgarøy, 1977) have been carried out with instruments sweeping over a broad bandwidth (narrow bandwidth) with low (high) frequency resolution. However, wide bandwidth studies with high resolution are necessary to understand the interplay between the various components comprising the storm radiation. Polarimetric observations over a wide band with high resolution will shed light on the characteristics of the plasma medium. This will also enable us to study both types of bursts associated with the noise storm, their associated continuum background emission, the transition region,[1] and their respective significance.

Recent advances in electronics have enabled the manufacture of data converters with better signal-to-noise ratio (S/N) and dynamic range, which allow the detection of faint bursts. Digital signal processing in high-speed field programmable gate Arrays (FPGA) provide real-time signal-processing capabilities such as polyphase filtering, fast Fourier transform, and integration operations. We exploit these advances to implement a wide-band, high-resolution instrument, which enabled us to observe the various components of storm radio emission distinctly, which has not been attempted or reported before. This is important from the point of view of understanding the relationship between storm burst and continuum radiation. The high spectral resolution of the instrument also allows us to flag channels corrupted by RFI more accurately, resulting in a minimum loss of spectral data. Keeping the above in mind, we designed an instrument, the *Low Frequency Spectropolarimeter* (LFSP), for conducting multifrequency polarimetric observations in the 15 MHz (the local ionospheric cutoff at Gauribidanur, Hariharan *et al.*, 2016) to 85 MHz band with $\approx 48\,\mathrm{kHz}$ spectral and 100 ms temporal resolution. We describe in detail the commissioning of the instrument and results from observations of a solar noise storm with it.

---

[1]By transition region, we mean the region corresponding to the plasma frequency where the Type I bursts "transition" to Type III bursts.

Figure 1 VSWR of antennas during an initial trial, with resistive stub and inductive stub. Note the improvement of VSWR in the operational band after the inclusion of the inductive stub.
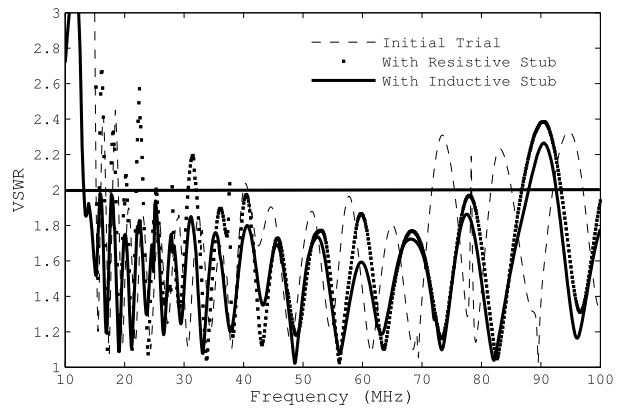
2. Low-frequency Spectropolarimeter Instrument

2.1. Antenna, Analog Front-End, and Array

An important parameter in choosing the necessary antenna architecture is the required operation bandwidth. Our goal was to study the characteristics of solar transients in metric and decametric wavelengths. The low-frequency cutoff will thus be the ionospheric cutoff frequency at Gauribidanur, which is ≈ 15 MHz. The high-frequency cutoff is decided by the frequency beyond which the terrestrial radio-frequency interference starts dominating the RF band, which in the present case is the FM transmissions (88 MHz – 108 MHz). Thus we chose our upper frequency cutoff to be ≈ 85 MHz. The required bandwidth ratio is $\approx 6:1$. This requires a frequency-independent antenna, whose electrical characteristics are to be identical throughout a wide range of frequencies.

We chose the log-periodic dipole antenna (LPDA) as our primary element because it is relatively easy to construct and has uniform gain characteristics throughout the band of interest. Standard techniques described by Raja *et al.* (2013), Kishore *et al.* (2014), and references therein were followed for the preliminary design of the LPDA. This initial design was repeatedly tuned to match the impedance throughout the operating band. We used an inductive stub to counter the capacitive reactance at low frequencies. The voltage standing-wave ratio (VSWR) of the antenna at various stages of design is shown in Figure 1. Note that between frequencies 15 MHz – 85 MHz, the VSWR is lower than two, which implies $\approx 90\%$ power transfer from source to load. The parameters of the designed LPDA are listed in Table 1.

The received signal from each antenna passes through an analog front-end (AFE) system. The AFE is composed of a five-stage high-pass (HPF) and low-pass filter (LPF) and an amplifier. The HPF is used to cut off strong low-frequency short-wave transmissions < 15 MHz. The LPF is used to cut off the FM band. The filtered signals are amplified by ≈ 30 dB. The characteristics of the filters and amplifier are shown in Figure 2.

The signal is then transmitted *via* phase-matched RG58U coaxial cables of length ≈ 50 m to the group center, where it is power combined with signals from other antennas of the group. The cables are phase matched to an accuracy of $\pm 2.5°$. The spacing between individual antennas in a group is ≈ 10 m. There are three such groups (see Table 2), of which two are oriented parallel to east–west (EW; 90° group), and the third is parallel to the north–south (NS; 0° group). The groups are laid out as an one-dimensional EW interferometer.

Table 1 Antenna parameters.

Parameters	Values
Number of arms	19
Apex angle	37°
Design constant (τ)	0.87
Spacing factor (σ)	0.032
Gain	5.5 dBi
E-plane HPBW	60°
H-plane HPBW	110°
Collecting area	$0.5\lambda^2$
VSWR in operating band	<2

Figure 2 Transfer characteristics of the LPF, HPF, and Amplifier.
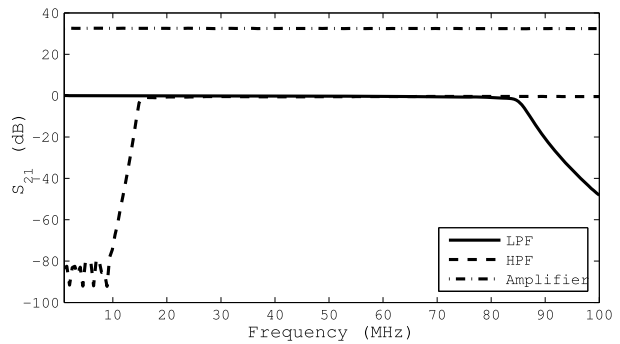
Figure 3 Schematic view of the AFE of a single group. The other groups also have a similar AFE setup.
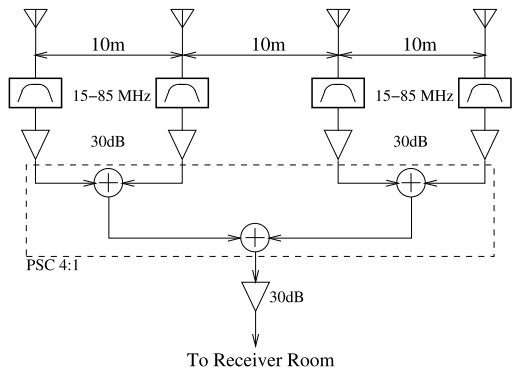
A schematic view of a single group with the AFE is shown in Figure 3. An image of a 90° group is shown in Figure 4.

The power-combined group signal is amplified by ≈ 30 dB and transmitted to the central receiving station *via* RG8U cables of varying lengths. These signals are amplified and filtered in the receiving station once more before digitization to i) compensate for cable loss and ii) attenuate out-of-band signals before they are input to the digital backend.

The mutual coherence between groups 1 and 3 is a measure of Stokes-V and that between group 2 and 3 is a measure of Stokes-I. The effective baseline lengths are ≈ 1.2 km. This

Table 2 Group parameters.

S. No.	Number of antennas	Orientation	Group extent [m]	Group HPBW
1	4	0°	30	1.91λ
2	4	90°	30	1.91λ
3	8	90°	70	0.82λ

Figure 4 Image of a single group. The antennas are nearly 6 m tall and 5 m wide. The smaller antennas on the far side are a part of the GRIP array.

is to remove all contribution from the extended corona and observe only transient energy releases.

2.2. Digital Receiver

The main task of the digital receiver is to process the received RF signal and estimate the Stokes parameters. The digital receiver is built around a CASPER[2] reconfigurable open-architecture computer hardware (ROACH) board. The first stage of the digital receiver is an analog to digital converter (ADC). A CASPER QADC is used for this purpose. QADC has four AD9480 eight-bit ADCs from analog devices.[3] These four ADCs share a common sampling clock. The maximum possible sampling clock is 250 MHz, which implies that a maximum baseband of 125 MHz can be sampled by the ADC. Since the band of interest here is 15 – 85 MHz, the sampling frequency used was 200 MHz.

The eight bits provide a dynamic range of ≈ 48 dB. This is sufficient to accommodate the increase in signal levels during solar bursts (Nelson, Sheridan, and Suzuki, 1985). The digitized signal is transmitted to further stages as a low-voltage differential signal (LVDS). LVDS signalling transmits a bit of data in two parallel lanes as in-phase and out-of-phase components. This reduces common mode noise in the digitized signal. In order to maintain synchronization with the digitizer, the data have to be captured by the LVDS receiver using the same clock frequency and phase. Therefore the sampling clock is also transmitted differentially from the ADC. Thus for an eight-bit ADC, there are 16 data lines and two clock lines. These lines are interfaced to ROACH using a ZDOK connector. The output signals are captured by the LVDS receivers present in the FPGA onboard the ROACH.

The firmware for the system was developed using CASPER's Matlab-Simulink-System-Generator-Embedded Development Kit (MSSGE) tool-flow. The ADC signal is converted

---

[2]See casper.berkeley.edu/.

[3]See www.analog.com/en/products/analog-to-digital-converters/ad-converters/ad9480.html.

from a signed integer into signed fixed-point number with 8.7 bit precision. This signal is then operated upon by a polyphase filter bank (Price, 2016; Crochiere and Rabiner, 1983; Vaidyanathan, 1993). PFB is a combination of a finite-impulse response (FIR) filter followed by an fast Fourier transform (FFT) operation. Polyphase filtering reduces spectral leakage into adjacent channels by ≈ 60 dB and reduces the data rate for further stages of processing. The FFT size is 4096, which resulted in a frequency resolution of ≈ 48.8 kHz. This frequency resolution enabled us to study finer frequency structures in radio emission from the Sun. It also helps us identify narrow-band RFI, which is confined to about two or three spectral channels, based on the bandwidth of the interfering signal. The outputs of the individual stages of the FFT are normalized to prevent bit growth and overflow during multiplication operations. Figure 5 shows that the inputs and outputs of the FFT block have the same bit width.

The spectrum of signals from each of the antennas are correlated to obtain the Stokes-I and Stokes-V visibilities. The destruction of linearly polarized components because of Faraday rotation in the solar corona for our spectral resolution means that we do not estimate or record the Stokes-Q and Stokes-U components (Ramesh *et al.*, 2008). The FFT and correlation operations are multiplication intensive, which results in bit growth of the output product. In order to prevent overflow, the spectra are therefore requantized to 8.7 bits before correlation. This bit resolution is sufficient to provide correlation that is $\approx 99\%$ of analog correlation (Thompson, Moran, and Swenson, 2001; Benkevitch *et al.*, 2016).

The quantizer output is fed to the Stokes estimators. The signals from groups 1 and 3 are correlated to estimate Stokes-I. The signals from groups 2 and 3 are correlated to obtain Stokes-V. Each Stokes estimator has a complex multiplier and an adder block. The output of the adder block is 17.14 bit wide. This output is integrated in the 32-bit wide vector accumulator (VACC).

The vector accumulator is implemented using block RAMs (BRAM) present in the FPGA. The depth of the accumulator is the same as the FFT size. Based on the desired temporal resolution, the number of spectra to be accumulated can be programmed by the observer during the initial configuration of the FPGA. When the predefined number of spectra has been accumulated, the VACC block generates a pulse, which indicates that the data are ready for processing at further stages.

The accumulated signal has to be prepared for transmission to the data-acquisition server (DAS). A ten Gb ethernet (10 Gbe) connection is used for communication to the DAS. A ten Gbe core, which is a part of CASPER toolflow, is used for this. The core accepts a 64-bit input. The input samples are stored in an elastic buffer,[4] which has a depth equal to the number of bytes (payload) to be transferred. The maximum payload size of 10 Gbe is 9000 bytes.

The data have to be packetized before transmission. The packetizer inputs are the integrated real and imaginary components that are output from the accumulators. The four first-in-first-out (FIFO) buffers in the packetizer module are used to capture the accumulated spectra synchronously from the VACC blocks. The size of each spectrum is $\approx$ eight kB (which is also the size of each FIFO); four spectra amount to ≈ 32 kB. However, the maximum payload capacity of 10 Gbe is only nine kB. Thus, the four spectra must be transmitted sequentially for smooth operation of the 10 Gbe core, without overflow of the transmit FIFO buffers.

After the last spectral sample is written to the FIFO, the FIFOFULL signal is asserted. On the assertion of this signal, the reading of spectrum data from the FIFO commences. After

[4]A FIFO buffer of variable size and read/write clocks.
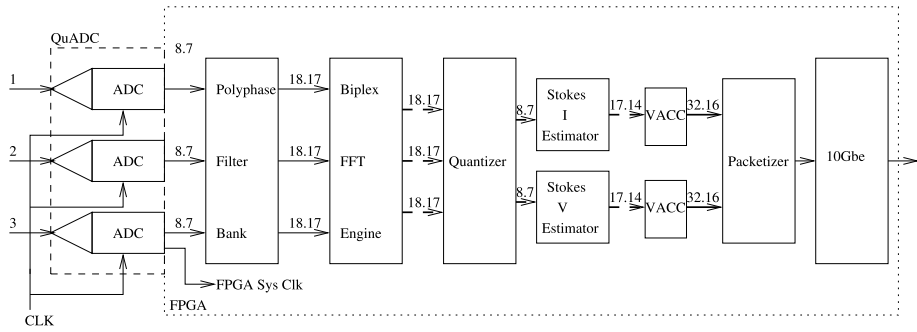
Figure 5 Architecture of the digital backend firmware. Numbers 1, 2, and 3 at the input are the respective antenna groups (see Table 2). Numbers of format $x.y$ represent the bit width of the signal being propagated to the next stage, x being the integer component, and y the fractional component. *Broken lines* represent complex numbers. In this case, the $x.y$ denotes the bit width of the real/imaginary part.

Table 3 Instrument parameters.

Parameter	Value
Primary element	Log Periodic Dipole Antenna (LPDA)
Operation frequency	$15 - 85$ MHz
Number of groups	3
Collecting area	$16\lambda^2$ (Stokes-I and Stokes-V)
Field of view	$\approx 0.82\lambda \times 90°$ (RA × Dec)
Spectral resolution	48.8 kHz
Time resolution	typ. 0.1 s (programmable)
Dynamic range	≈ 48 dB

reading out the first FIFO completely, a delay is provided before the second FIFO is read out. This is to ensure that the 10 Gbe core does not malfunction between data transmissions. The packetizer control state machine was implemented in Simulink using a Matlab M-code block. On the DAS, a shell script is written to configure, control, and acquire data during observation. Each set of four spectra is output as four 10 Gbe packets for a single integration time. The delay between subsequent packets is $\approx$ five μs.

The digital receiver architecture is shown in Figure 5. A summary of the polarimeter parameters is given in Table 3.

2.3. Calibration

Calibration of polarimeters is usually carried out by feeding a switched noise input at the antenna feed, feeding noise from another antenna that is located higher than the array to be calibrated, or using drones (Pupillo *et al.*, 2015). However, the extent of the array (≈ 1.2 km) prevented implementing these techniques for polarization calibration in our case. A strong unpolarized calibrator source such as Cygnus A can be used to set the flux scale for Stokes-I and also to estimate the instrumental polarization (Sault, Hamaker, and Bregman, 1996). Moreover, the high radio brightness of Cygnus A ($\gtrsim 15000$ Jy in $15 - 85$ MHz) means that it can be used to unambiguously calibrate observations with high temporal resolution (≈ 0.1 s).

The deflection obtained for Cygnus A in Stokes-V can be used to remove instrumental polarization that arises from the mutual coupling between antennas, spurious ground reflections, polarization induced by signal path, *etc*.

The Stokes-I and Stokes-V solutions obtained for the calibrator can be directly applied to solar observations to estimate the flux and the error in degree of circular polarization (dcp) of solar transients. The extended emission from the background is completely resolved because of the baseline lengths involved, and mutual coupling between Stokes-I and Stokes-V interferometers is minimized. We also use this instrument to carry out transit observations alone, thus avoiding errors that depend on source position.

3. Observations

The noise-storm observation presented here was carried out during 18 – 19 June 2016. This storm was found to be associated with AR12567. The mutual coherence between two groups of antennas oriented in the same direction yielded Stokes-I, while that of two groups oriented orthogonally was used to estimate Stokes-V. LFSP operates in the frequency range of 15 – 85 MHz. The temporal resolution of the data is ≈ 0.1 second, and the spectral resolution is ≈ 48 kHz. The Stokes-I and Stokes-V dynamic spectra observed on 19 July 2016, obtained using LFSP, are shown in Figure 6.

We also used imaging data from the *Gauribidanur RAdio HeliograPH* (GRAPH: Ramesh *et al.*, 1998; Ramesh, Sundararajan, and Sastry, 2006; Ramesh, Kathiravan, and Narayanan, 2011) to obtain 2D radio images of the corona. GRAPH images the Sun at two interference-free spot frequencies (53.3 MHz and 80 MHz) with a temporal resolution of one second. The angular resolution of the final maps is $5' \times 7'$ and $7' \times 9'$ at 80 MHz and 53.3 MHz, respectively. A 2D image of the active region at 80 MHz and 53.3 MHz obtained using GRAPH is shown in Figure 8. The GRAPH images are used to infer the heights of the source regions above the corona and to estimate the density model.

We used a dynamic spectrum obtained with the *Gauribidanur Low Frequency Solar Spectrograph* (GLOSS: Ebenezer *et al.*, 2001; Kishore *et al.*, 2014) to determine the highest frequency at which Type I and Type III bursts were observed during the observation days. GLOSS is a phased array of eight antennas oriented N–S. The response of GLOSS has to be electrically tilted in the declination axis to point the instrument toward the Sun. The broad response of GLOSS in RA enables observation of the Sun for up to eight hours per day. GLOSS operates in a frequency band of 40 – 440 MHz with a spectral resolution of 1 MHz and a temporal resolution of 250 ms.

The data used for this observation were obtained for ≈ 30 minutes about the local meridian transit of the Sun using the LFSP. This was done to i) avoid confusion arising due to the array side-lobes and grating-lobes at higher frequencies and ii) minimize errors in polarization due to parallactic angle. Cygnus A observations performed on the same day were used for flux calibration and to remove errors arising due to instrumental polarization.

The GRAPH images were made at both the frequencies by integrating the visibilities for $\pm$ ten seconds about the meridian transit. The GRAPH images were also calibrated using Cygnus A. An inspection of the GRAPH images at both frequencies reveal a compact source on the disk, which is the storm source region.

From the spectropolarimeter observations, we chose only isolated Type I bursts for further analysis (left panel in Figure 7). The bursts that were part of a chain, of a drifting chain, or those that appeared to be indistinguishable from the background were not considered for analysis. Similarly, Type III bursts that showed peculiar drifts or on which some other features were superimposed were not considered.

Figure 6 Dynamic spectrum of Stokes-*I* (*top*) and Stokes-*V* (*bottom*) of the noise storm obtained using the LFSP. The spot-like features are Type I bursts, the vertical stripe-like features are Type III bursts. The *horizontal lines* are due to narrow-band RFI.
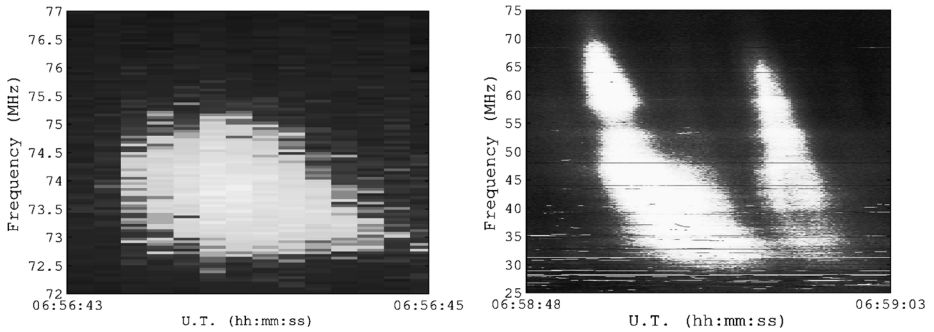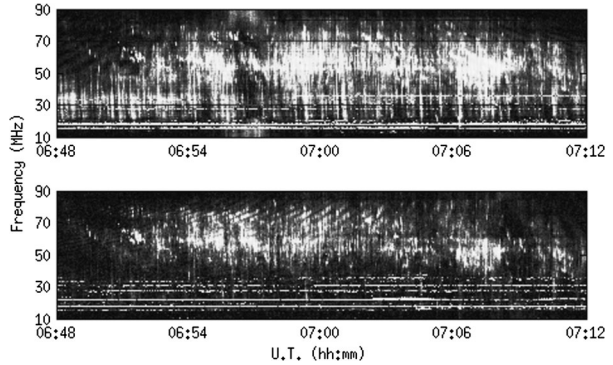
Figure 7 Sample of isolated Type I (*left*) and Type III bursts.

4. Analysis and Results

From the Stokes-*I* spectrum (top panel in Figure 6), we observe that at lower frequencies, the bright background and spot-like features (Type I bursts) are not visible. Storm observations in the past have indicated the existence of a transition frequency around which the Type I bursts transcend to Type III bursts (see Section 1). Type III bursts are broad-band short-lived emission excited by an electron beam traversing the plasma layers at relativistic velocities. Keeping this in view, we carried out a statistical analysis of the data. We used the fractional bandwidth as a figure of merit to study the spectral characteristics of the Type I and Type III bursts. The fractional bandwidth is defined as the ratio of the bandwidth of the burst to the ratio of the center frequency.

A MATLAB program was used to semi-automatically detect individual bursts. The detected bursts were integrated in time to obtain the frequency profile. A Gaussian of the form $a \exp\left(-((f - f_c)/\delta f)^2\right)$, where f_c is the center frequency, δf is the bandwidth of the burst, and a is the peak amplitude, was fitted to the obtained frequency profiles of the Type I bursts. For Type III bursts, the frequencies of the first and last appearance were used to estimate the fractional bandwidth. For both days, we obtained $\gtrsim 100$ individual Type I and Type III bursts. We found that the lower cutoff of Type I bursts occurred around ≈ 50 MHz. The bursts were observed up to the high-frequency cutoff of the instrument. The bursts were well dispersed in time and frequency planes. Type III bursts had a fractional bandwidth in the range of 0.4 to 1.2. A scatter plot of fractional bandwidth and center frequency of Type I and Type III bursts is shown in Figure 10. The transition frequency occurs at ≈ 53 MHz.
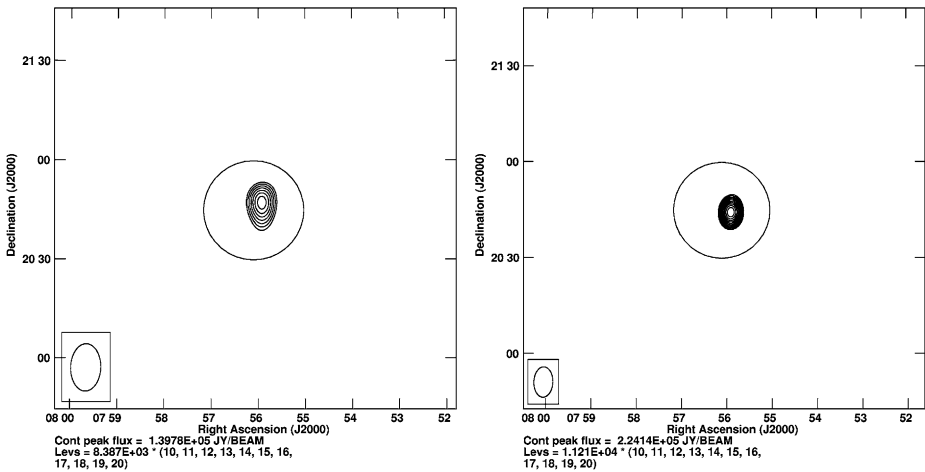
Figure 8 GRAPH images at 53.5 MHz (*left*) and 80 MHz. The *circle* denotes the solar photospheric disk. The *contours* indicate a noise-storm source close to the disk center. The flux at 80 MHz is greater than that at 53.3 MHz.

Based on this result, we carried out further analysis of the bursts and the continuum background to study the characteristics of these bursts in detail and also to identify any change in the radio-emission characteristics above and below the transition frequency.

For the continuum analysis, we used the temporal intensity variation profile at the frequencies of interest. The lower envelope of the profile was used as the continuum background (see Figure 9). This is justified if the storm continuum is considered as a broad-band long-lived background over which bursts are superposed. The single source in the radio image indicates that continuum emission at high and low frequencies alike arises from the same region. On detailed analysis of the continuum profiles obtained at different frequencies, we found that the spectral indices of metric continuum ($\gtrsim 50$ MHz) were different from those of the decametric continuum ($\lesssim 50$ MHz). By fitting a power law to the flux as a function of frequency, we found that the spectral indices for the metric and decametric continuum were $+2.9$ and -1.6, respectively (see Figures 11 and 12). This also sets an upper limit on the extent of the Type I continuum source region.

Since the bursts were dispersed in time and frequency, we used the amplitude and frequency of all of the observed bursts as they belonged to the same burst complex to study the spectral index of Type I bursts. By fitting a power law to the above distribution, we found that the spectral index of Type I bursts was $\approx +3.4$ (see Figure 13). The trend in frequency shown by the flux of Type I bursts and of the metric continuum are similar.

We used the Type III bursts observed during the two days to study the spectral characteristics of the bursts. The flux for different bursts at frequencies within the upper and lower cutoff was estimated from their individual time profiles. A power-law curve was fit for the flux as a function of frequency for all the bursts. For all of the Type III bursts, the flux decreased with frequency. The mean spectral index was -2.7 ± 0.2 (see Figure 14). Similar to Type I burst and continuum, Type III burst and continuum also show the same spectral variation.

From the inspection of the Stokes-*V* dynamic spectrum (bottom panel in Figure 6), we see that at low frequencies, the circularly polarized intensity decreases. We therefore carried out an analysis of the degree of circular polarization (dcp) for the Type I and Type III bursts.

Figure 9 Continuum background at 55 MHz (*solid line*). Fluctuation in the received power during the storm (*dots*).
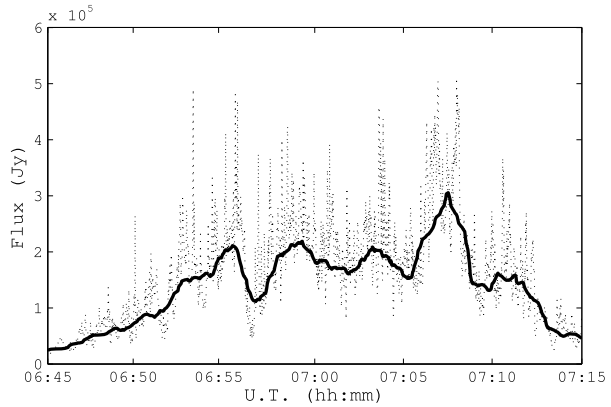
Figure 10 Scatter of fractional bandwidth and center frequency of bursts. The Type I bursts disappear at frequencies < 50 MHz.
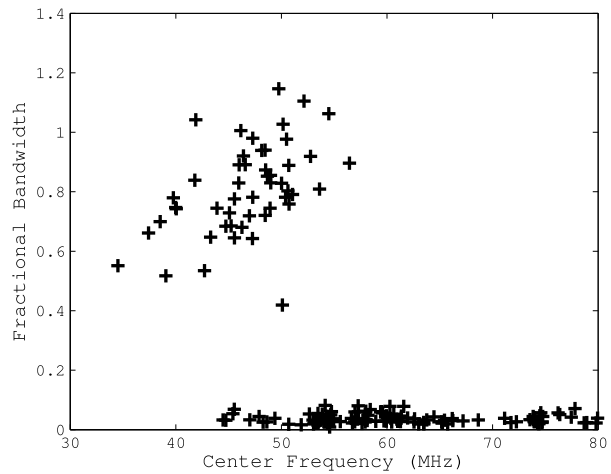

We defined dcp as the absolute value of the ratio of Stokes-I and Stokes-V fluxes. For Type I bursts, we estimated the dcp as the ratios of the peak of the Gaussian fit for Stokes-I and Stokes-V. For Type III bursts, the peak values at the center frequency of the burst were used for the dcp calculation. From the distribution of the dcp (see Figure 15), we see that Type I bursts are more polarized than Type III bursts. The minimum percent of the dcp for Type I bursts is $\approx 55\%$, while most Type I bursts are strongly polarized (dcp $\gtrsim 90\%$). On the other hand, Type III bursts were only moderately polarized. Out of the observed bursts, only $\approx 50\%$ showed any detectable Stokes-V deflection. The distribution of the dcp for these bursts is shown in Figure 16.

5. Discussion

Using the result of the analysis presented in the previous section, we propose a possible scenario for the observed characteristics (see Figure 17). Noise storm emission is generally thought to emanate from electron acceleration in closed magnetic arches. The exact mechanism of the electron acceleration is not known. Since the corona is a plasma medium, the
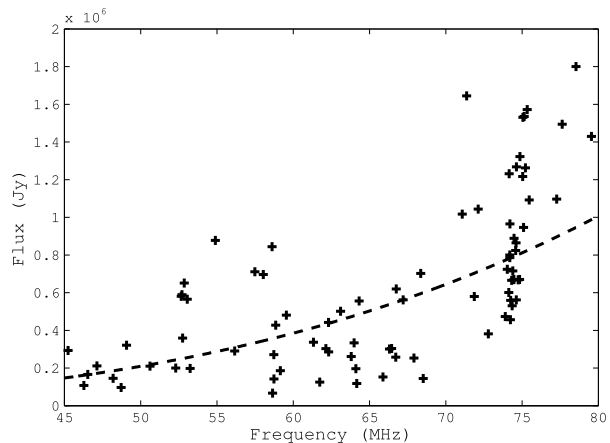
Figure 11 Spectral index of the metric continuum. The *dashed line* shows a power-law fit of index +2.9.
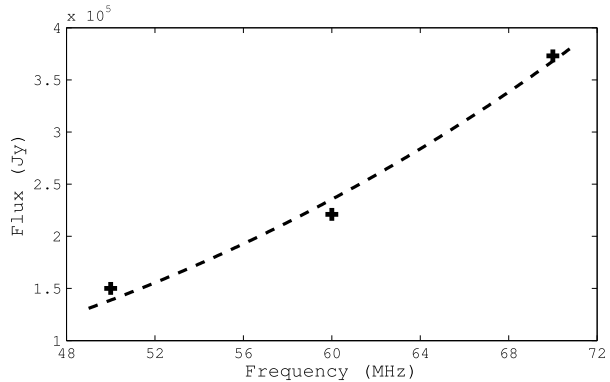
Figure 12 Spectral index of the decametric continuum. The *dashed line* shows a power-law fit of index −1.6.
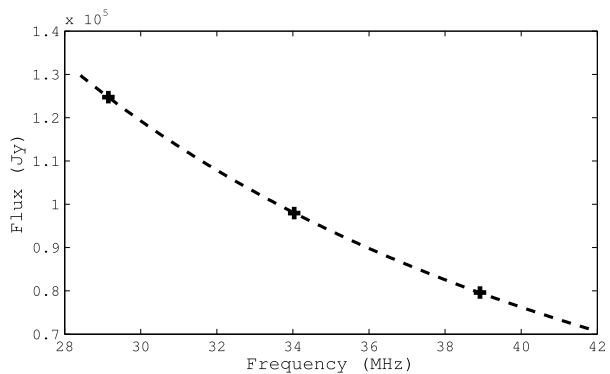

Figure 13 Spectral index of Type I bursts. The *dashed line* shows a power-law fit of index +3.4.


laws governing propagation through a plasma dictate that electromagnetic radiation occurring at a frequency [f] must originate at or near regions of plasma frequency [f]. Inspection of GLOSS data for the duration of the noise storm revealed that beyond 220 MHz, no Type I activity occurred. From the low frequency spectropolarimeter observations, we also see that there was no Type I emission at frequencies $\lesssim 50$ MHz.
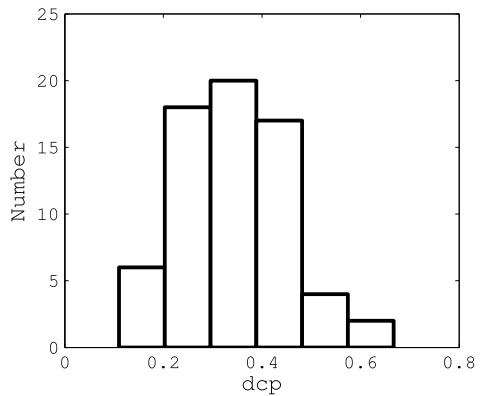
Figure 14 Spectral index
distribution of Type III bursts.
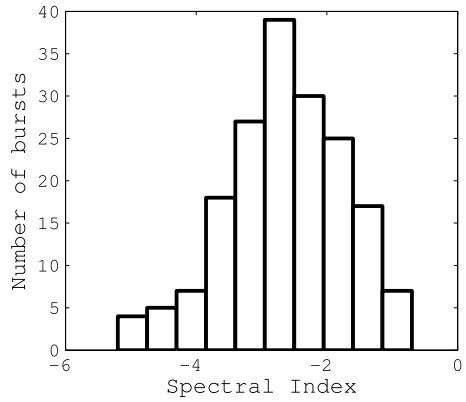
Figure 15 The dcp distribution
of Type I bursts.
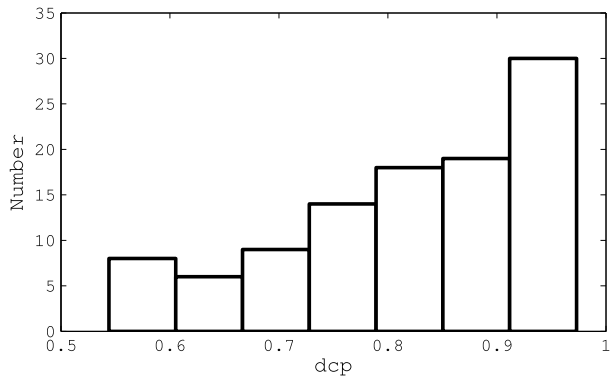
Figure 16 The dcp distribution
of Type III bursts.

With an appropriate density model, the extent of the Type I source region can therefore
be constrained. We used the heliograph images for this. We estimated the rotation rate [β]
of the sources at the two frequencies. From this, the radial distance [r] can be estimated
using the relation $r\phi = D\beta$, where $\phi \approx 13.3°$ is the angular displacement of the associated
active region on the solar disk per day and D is the Sun–Earth distance, which is $\approx 215R_\odot$
(Ramesh, Kathiravan, and Narayanan, 2011). The estimated radial distances and frequencies

were then used to numerically solve to find an appropriate density model. The Baumbach–Allen density model with an enhancement factor of two provided the closest match, with a minimized least-squares error, to the radial distances obtained from the previous step. Based on this, we find that the Type I source region extends from $1.03R_\odot$ to $1.51R_\odot$.

Based on the results obtained from our spectral index analysis of Type I continuum and bursts described in Section 4, we find that they both have a positive spectral index. The positive spectral index obtained for the continuum and bursts are consistent with previous results reported by Sundaram and Subramanian (2004) in the $50–80$ MHz range and Iwai *et al.* (2012) at frequencies greater than 100 MHz. This gives us confidence in the approach that we used for the analysis. We therefore suggest that Type I bursts and continuum have the same emission mechanism. Numerous indistinguishable Type I bursts of different energy levels form the continuum emission. These bursts, which are brighter than the continuum (but are still a part of the continuum) are observed as Type I bursts. Plasma emission from suprathermal electrons (Thejappa, 1991) is the cause of Type I bursts. The finite bandwidth and time of these bursts can be explained as fluctuations in the suprathermal electron density.

We find from GLOSS observations on $18–19$ July 2016 that the Type III bursts coinciding with our time of observation were restricted at frequencies < 100 MHz. The start frequencies of these bursts are around $50–60$ MHz. This shows that Type III bursts observed during storms also originate from the Type I source region. It also indicates that the open magnetic-field lines along which Type III electrons travel originate at the height range corresponding to the above frequency range. The fact that no Type III burst was observed to originate from frequencies $\gtrsim 220$ MHz during the observation time of the LFSP indicates that all of the Type III bursts observed are indeed associated with the noise-storm radio emission region (Gergely and Erickson, 1975; Gergely and Kundu, 1975). The Type III start frequencies are close to the cutoff frequency of the Type I storm emission, which suggests that these Type III electrons are beamed from regions close to the edge of the Type I source. Thus, the claim that Type III bursts observed during noise storms arise from the same electron population as Type I bursts may seem plausible, if we constrain Type III bursts to originate from escaping electrons that are close to the cusp of the magnetic arch. Type III electrons may be left-over electrons that were responsible for Type I bursts, which escape from the magnetic arches at a lower velocity into the open field lines, thus exciting the plasma layers there, and manifest as Type III bursts. Noise storms have also been found to give rise to weak energy releases such as nano- and pico-flares (Mercier and Trottet, 1997; Ramesh *et al.*, 2013). We speculate that these weak-energy releases could accelerate the left-over electrons to produce Type III bursts.

The spectral-index values obtained for the Type III continuum and bursts are -1.6 and -2.7, respectively. This suggests that the continuum may just be an agglomeration of Type III bursts occurring in rapid succession. Since the Type III continuum is observed only at $\lesssim 50$ MHz, this is an indication that the emission regions of Type I and Type III continuum do not overlap.

We also find that Type I bursts are more polarized than Type III bursts. Magneto-ionic theory describes two modes of wave propagation: ordinary mode (o-mode), and extra-ordinary mode (e-mode). The cutoff frequency of the o-mode is at $\omega_{\rm p}$, while that of the e-mode is at $\frac{1}{2}(-\omega_{\rm e} + \sqrt{\omega_{\rm e}^2 + 4\omega_{\rm p}^2})$, where $\omega_{\rm p}$ is the electron plasma frequency and $\omega_{\rm e}$ is the electron gyro-frequency. These equations show that the e-mode cutoff occurs higher in the corona than the o-mode cutoff. All of the radiation emitted by the source at frequency $< \omega_{\rm p}$ will not escape, and thus no radiation will be observed. Radiation from the source emitted at frequencies between the o-mode and the e-mode cutoff frequencies will escape with polarization at the o-mode and will have a strong circularly polarized signature. Radiation emitted

Figure 17 Scenario suggested for unified Type I and Type III storm emission. The *hatched region* is the region from which the Type I radiation originates. The radiation extends throughout the open field lines. The Type I radiation originates from the region that is constrained between the two *lines* representing the upper and lower storm-radiation cutoffs as obtained from GLOSS and the spectropolarimeter, respectively. The *hatched circles* are the positions of storm source region as observed from GRAPH. See Section 5 for their positions.
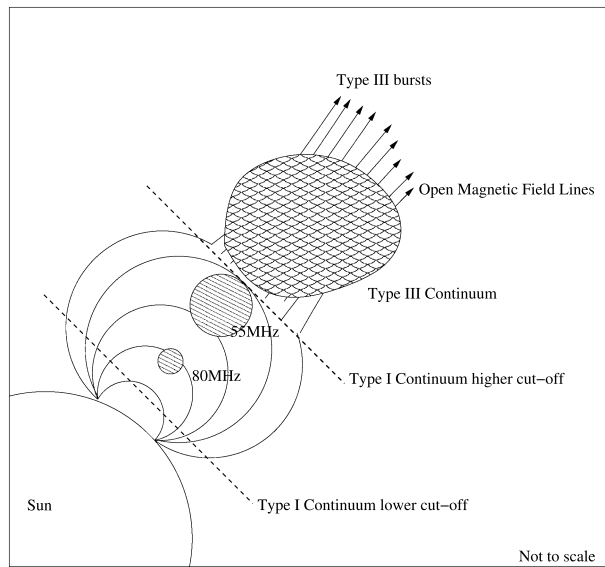
at frequencies greater than the o-mode and e-mode cut-off will escape with either mode, but the net polarization will be lower. The above theory can be applied to Type I bursts. If Type I bursts emanate from plasma layers with a cutoff frequency between that of the o-mode and e-mode frequencies, then one would expect to measure high degrees of circular polarization, similar to what we measured here. This suggests that Type I bursts may be a result of fundamental plasma emission.

For the polarization of Type III bursts, we detect low polarization values ($\approx 25\%$), which is consistent with what has been reported for fundamental Type III emission (Dulk and Suzuki, 1980; Sasikumar Raja and Ramesh, 2013). The low polarization values can be due to mixing of magneto-ionic modes, which would result in a net decrease of the dcp.

We note here that because of the wide instantaneous bandwidth, we were able to obtain simultaneous observations of Type I and Type III storm radio emission. With the superior spectral and temporal resolutions, we are able to distinguish between the continuum and burst components of each emission type. We also find that the nature of the polarization of Type I and Type III bursts is entirely different, a deduction that was possible because of the spectropolarimetric capabilities of the instrument. This has enabled us to constrain the properties of the Type I and Type III bursts and their continuum.

6. Summary and Scope

We presented high-resolution, calibrated, spectropolarimetric observations of solar noise storms using a purpose-built interferometric polarimeter. The high spectral and temporal resolutions allowed us to resolve a higher number of bursts and derive statistics out of it. Moreover, the wide frequency coverage enabled us to study Type I and Type III noise storm phenomena. By studying the spectral characteristics of the noise storms, we find the following:

  i) Type I bursts occurring in rapid succession form the continuum at frequencies $\gtrsim 50$ MHz.

ii) Type III bursts occurring in rapid succession form the continuum at frequencies $\lesssim 50$ MHz.

iii) We also estimate the transition frequency between Type I and Type III bursts and locate the height range from which open magnetic-field lines emerge.

iv) The dcp measurements indicate that Type I storms are more polarized than Type III storms, implying that the former occurs in more magnetically dense regions.

Based on these discussions, we assert observationally that Type I and Type III storms are both due to plasma emission. Acceleration of suprathermal electrons in magnetic arches may be attributed to the former, based on its spectral properties, while the latter could be due to the same population of electrons, but at a decreased velocity, exciting plasma layers when traveling outward in open-field lines. The high degree of polarization is explained as a consequence of Type I being solely caused by o-mode, but Type III storms show lower polarization as a result of mode mixing. We also find that the continuum associated with the respective bursts is a coalescence of many such unresolved bursts. Our conclusions here lead to an important question: if both Type I and Type III bursts arise from the same population of electrons and the emission mechanism is also fundamental plasma emission, what causes the striking difference in their spectral and polarization characteristics? A second question is whether all noise storms have similar spectropolarimetric characteristics. Future high-resolution imaging observations in the frequency range of $15 - 300$ MHz (in Stokes-*I* and Stokes-*V*) with an angular resolution of $\leq 1'$ could prove useful in studying the evolution of Type I and Type III storm radiation (Melrose, 1980; Benz and Wentzel, 1981; Kerdraon *et al.*, 1983; Ramesh, Subramanian, and Sastry, 1999; Kathiravan *et al.*, 2011; Mugundhan *et al.*, 2016). An instrument with sensitivity to weaker energy releases (Ramesh *et al.*, 2010; Oberoi *et al.*, 2011) is preferable since it would help in understanding the energy budgets of Type I and Type III storms. Synchronous observations using space-based telescopes and ground-based radio telescopes such as GRAPH (www.iiap.res.in/centers/radio/), the *LOw Frequency ARray* (LOFAR: van Haarlem *et al.*, 2013), the *Long Wavelength Array* (LWA: Ellingson *et al.*, 2009), and the *Murchison Widefield Array* (MWA: Tingay *et al.*, 2013), which would provide an almost continuous coverage of the measurable electromagnetic spectrum, are expected to yield a better understanding of the storm phenomena.

Disclosure of Potential Conflicts of interest   We declare that there are no conflicts of interest for the work presented here.

References

Allen, C.W.: 1947, Solar radio-noise of 200 mc./s. and its relation to solar observations. *Mon. Not. Roy. Astron. Soc.* **107**(4), 386. DOI. mnras.oxfordjournals.org/content/107/4/386.abstract.

Benkevitch, L.V., Rogers, A.E.E., Lonsdale, C.J., Cappallo, R.J., Oberoi, D., Erickson, P.J., Baker, K.A.V.: 2016, Van Vleck correction generalization for complex correlators with multilevel quantization. ADS.

Benz, A.O., Wentzel, D.G.: 1981, Coronal evolution and solar type i radio bursts – an ion-acoustic wave model. *Astron. Astrophys.* **94**, 100. ADS.

Boischot, A., de La Noe, J., Moller-Pedersen, B.: 1970, Relation between metric and decametric noise storm activity. *Astron. Astrophys.* **4**, 159. ADS.

Crochiere, R.E., Rabiner, L.R.: 1983, *Multirate Digital Signal Processing*, 4th edn., *Prentice-Hall Signal Processing Series: Advanced Monographs* **1**, Prentice Hall, Upper Saddle River.

de La Noe, J., Gergely, T.E.: 1977, The spectrum and position of solar noise storms at decameter wavelengths. *Solar Phys.* **55**, 195. DOI. ADS.

Dodson, H.W.: 1957, Relation between optical solar features and solar radio emission. In: van de Hulst, H.C. (ed.) *Radio Astronomy*, *IAU Symposium* **4**, 327. ADS.

Dulk, G.A., Suzuki, S.: 1980, The position and polarization of Type III solar bursts. *Astron. Astrophys.* **88**, 203. ADS.

Ebenezer, E., Ramesh, R., Subramanian, K.R., Sundara Rajan, M.S., Sastry, C.V.: 2001, A new digital spectrograph for observations of radio burst emission from the Sun. *Astron. Astrophys.* **367**, 1112. ADS.

Elgarøy, E.Ø.: 1977, *Solar noise storms*. ADS.

Ellingson, S.W., Clarke, T.E., Cohen, A., Craig, J., Kassim, N.E., Pihlstrom, Y., Rickard, L.J., Taylor, G.B.: 2009, The long wavelength array. *Proc. IEEE* **97**(8), 1421.

Gergely, T.E., Erickson, W.C.: 1975, Decameter storm radiation. I. *Solar Phys.* **42**, 467. DOI. ADS.

Gergely, T.E., Kundu, M.R.: 1975, Decameter storm radiation. II. *Solar Phys.* **41**, 163. DOI. ADS.

Hariharan, K., Ramesh, R., Kathiravan, C., Abhilash, H.N., Rajalingam, M.: 2016, High dynamic range observations of solar coronal transients at low radio frequencies with a spectro-correlator. *Astrophys. J. Suppl.* **222**(2), 21. stacks.iop.org/0067-0049/222/i=2/a=21.

Hey, J.S., Parsons, S.J., Phillips, J.W.: 1948, Some characteristics of solar radio emissions. *Mon. Not. Roy. Astron. Soc.* **108**, 354. DOI. ADS.

Iwai, K., Tsuchiya, F., Morioka, A., Misawa, H.: 2012, IPRT/AMATERAS: a new metric spectrum observation system for solar radio bursts. *Solar Phys.* **277**, 447. DOI. ADS.

Kathiravan, C., Ramesh, R., Nataraj, H.S.: 2007, The post-coronal mass ejection solar atmosphere and radio noise storm activity. *Astrophys. J. Lett.* **656**, L37. DOI. ADS.

Kathiravan, C., Ramesh, R., Indrajit, V. Barve, Rajalingam, M.: 2011, Radio observations of the solar corona during an eclipse. *Astrophys. J.* **730**, 91. ADS.

Kerdraon, A., Pick, M., Trottet, G., Sawyer, C., Illing, R., Wagner, W., House, L.: 1983, The association of radio noise storm enhancements with the appearance of additional material in the corona. *Astrophys. J. Lett.* **265**, L19. ADS.

Kishore, P., Kathiravan, C., Ramesh, R., Rajalingam, M., Barve, I.V.: 2014, Gauribidanur low-frequency solar spectrograph. *Solar Phys.* **289**(10), 3995. DOI.

McCready, L.L., Pawsey, J.L., Payne-Scott, R.: 1947, Solar radiation at radio frequencies and its relation to sunspots. *Proc. Roy. Soc. London Ser. A, Math. Phys. Sci.* **190**, 357. DOI. ADS.

Melrose, D.B.: 1980, A plasma-emission mechanism for type i solar radio emission. *Solar Phys.* **67**, 357. ADS.

Mercier, C., Trottet, G.: 1997, Coronal radio bursts: a signature of nanoflares? *Astrophys. J. Lett.* **474**(1), L65. stacks.iop.org/1538-4357/474/i=1/a=L65.

Mugundhan, V., Ramesh, R., Barve, I.V., Kathiravan, C., Gireesh, G.V.S., Kharb, P., Misra, A.: 2016, Low-frequency radio observations of the solar corona with arcminute angular resolution: implications for coronal turbulence and weak energy releases. *Astrophys. J.* **831**, 154. DOI. ADS.

Nelson, G.J., Sheridan, K.V., Suzuki, S.: 1985, Measurements of solar flux density and polarization. In: McLean, D.J., Labrum, N.R. (eds.) *Solar Radiophysics: Studies of Emission from the Sun at Metre Wavelengths*, Cambridge University Press, Cambridge, 113. ADS.

Oberoi, D., Matthews, L.D., Cairns, I.H., Emrich, D., Lobzin, V., *et al.*: 2011, First spectroscopic imaging observations of the sun at low radio frequencies with the Murchison Widefield Array prototype. *Astrophys. J. Lett.* **728**, L27. ADS.

Payne-Scott, R.: 1949, Bursts of solar radiation at metre wavelengths. *Aust. J. Sci. Res., Ser. A* **2**, 214. ADS.

Price, D.C.: 2016, Spectrometers and polyphase filterbanks in radio astronomy. arXiv. ADS.

Pupillo, G., Naldi, G., Bianchi, G., Mattana, A., Monari, J., Perini, F., Poloni, M., Schiaffino, M., Bolli, P., Lingua, A., Aicardi, I., Bendea, H., Maschio, P., Piras, M., Virone, G., Paonessa, F., Farooqui, Z., Tibaldi, A., Addamo, G., Peverini, O.A., Tascone, R., Wijnholds, S.J.: 2015, Medicina array demonstrator: calibration and radiation pattern characterization using a UAV-mounted radio-frequency source. *Exp. Astron.* **39**, 405. DOI. ADS.

Raja, K.S., Kathiravan, C., Ramesh, R., Rajalingam, M., Barve, I.V.: 2013, Design and performance of a low-frequency cross-polarized log-periodic dipole antenna. *Astrophys. J. Suppl.* **207**(1), 2. stacks.iop.org/0067-0049/207/i=1/a=2.

Ramesh, R., Kathiravan, I.C., Rajalingam, M.: 2012, High angular resolution radio observations of a coronal mass ejection source region at low frequencies during a solar eclipse. *Astrophys. J.* **744**, 165. ADS.

Ramesh, R., Kathiravan, C., Narayanan, A.S.: 2011, Low-frequency observations of polarized emission from long-lived non-thermal radio sources in the solar corona. *Astrophys. J.* **734**(1), 39. stacks.iop.org/0004-637X/734/i=1/a=39.

Ramesh, R., Shanmugha Sundaram, G.A.: 2001, Occurrence of metric noise storms and the onset of coronal mass ejections in the solar atmosphere. *Solar Phys.* **202**, 355. ADS.

Ramesh, R., Subramanian, K.R., Sastry, C.V.: 1999, Eclipse observations of compact sources in the outer solar corona. *Solar Phys.* **185**, 77. ADS.

Ramesh, R., Sundararajan, M.S., Sastry, C.V.: 2006, The 1024 channel digital correlator receiver of the Gauribidanur radioheliograph. *Exp. Astron.* **21**, 31. DOI. ADS.

Ramesh, R., Subramanian, K.R., Sundararajan, M.S., Sastry, C.V.: 1998, The Gauribidanur Radioheliograph. *Solar Phys.* **181**, 439. DOI. ADS.

Ramesh, R., Kathiravan, C., SundaraRajan, M.S., Barve, I.V., Sastry, C.V.: 2008, A low-frequency (30 – 110 MHz) antenna system for observations of polarized radio emission from the solar corona. *Solar Phys.* **253**(1), 319. DOI.

Ramesh, R., Kathiravan, C., Barve, I.V., Beeharry, G.K., Rajasekara, G.N.: 2010, Radio observations of weak energy releases in the solar corona. *Astrophys. J. Lett.* **719**, L41. ADS.

Ramesh, R., Sasikumar Raja, K., Kathiravan, C., Satya Narayanan, A.: 2013, Low-frequency radio observations of picoflare category energy releases in the solar atmosphere. *Astrophys. J.* **762**, 89. ADS.

Ryle, M.: 1948, The generation of radio-frequency radiation in the sun. *Proc. Roy. Soc. London Ser. A, Math. Phys. Sci.* **195**(1040), 82. www.jstor.org/stable/98304.

Sasikumar Raja, K., Ramesh, R.: 2013, Low-frequency observations of transient quasi-periodic radio emission from the solar atmosphere. *Astrophys. J.* **775**, 38. ADS.

Sault, R.J., Hamaker, J.P., Bregman, J.D.: 1996, Understanding radio polarimetry. II. Instrumental calibration of an interferometer array. *Astron. Astrophys. Suppl. Ser.* **117**, 149. ADS.

Stewart, R.T., Labrum, N.R.: 1972, Meter-wavelength observations of the solar radio burst storm of August 17 – 22, 1968. *Solar Phys.* **27**, 192. DOI. ADS.

Sundaram, G.A.S., Subramanian, K.R.: 2004, Spectrum of solar Type I continuum noise storm in the 50 – 80 MHz band and plasma characteristics in the associated source region. *Astrophys. J.* **605**, 948. DOI. ADS.

Swarup, G., Stone, P.H., Maxwell, A.: 1960, The association of solar radio bursts with flares and prominences. *Astrophys. J.* **131**, 725. DOI. ADS.

Thejappa, G.: 1991, A self-consistent model for the storm radio emission from the sun. *Solar Phys.* **132**, 173. DOI. ADS.

Thompson, A.R., Moran, J.M., Swenson, G.W.: 2001, *Interferometry and Synthesis in Radio Astronomy*, 2nd edn., Wiley-VCH, Weinheim. cds.cern.ch/record/1320565.

Tingay, S., Goeke, R., Bowman, J.D., Emrich, D., Ord, S., Mitchell, D.A., Morales, M.F., Booler, T., Crosse, B., Wayth, R., *et al.*: 2013, The Murchison Widefield Array: The Square Kilometre Array precursor at low radio frequencies. *Publ. Astron. Soc. Austral.* **30**, e007.

Vaidyanathan, P.P.: 1993, *Multirate Systems and Filter Banks*, **1**, Prentice Hall, Upper Saddle River. 0-13-605718-7.

van Haarlem, M., Wise, M., Gunst, A., Heald, G., McKean, J., Hessels, J., de Bruyn, A., Nijboer, R., Swinbank, J., Fallows, R., *et al.*: 2013, Lofar: the low-frequency array. *Astron. Astrophys.* **556**, 2.

Wild, J.P.: 1951, Observations of the spectrum of high-intensity solar radiation at metre wavelengths. IV. Enhanced radiation. *Aust. J. Sci. Res., Ser. A* **4**, 36. ADS.

Wild, J.P., McCready, L.L.: 1950, Observations of the spectrum of high-intensity solar radiation at metre wavelengths. I. The apparatus and spectral types of solar burst observed. *Austral. J. Sci. Res., Ser. A* **3**, 387. ADS.

Zlobec, P.: 1971, Polarization of type I bursts. In: Abrami, A. (ed.) *CESRA-2, Comm. European Solar Radio Astron.* **2**, 101. ADS.